

REPORT DOCUMENTATION PAGE			Form Approved OMB NO. 0704-0188	
<p>The public reporting burden for this collection of information is estimated to average 1 hour per response, including the time for reviewing instructions, searching existing data sources, gathering and maintaining the data needed, and completing and reviewing the collection of information. Send comments regarding this burden estimate or any other aspect of this collection of information, including suggestions for reducing this burden, to Washington Headquarters Services, Directorate for Information Operations and Reports, 1215 Jefferson Davis Highway, Suite 1204, Arlington VA, 22202-4302. Respondents should be aware that notwithstanding any other provision of law, no person shall be subject to any penalty for failing to comply with a collection of information if it does not display a currently valid OMB control number.</p> <p>PLEASE DO NOT RETURN YOUR FORM TO THE ABOVE ADDRESS.</p>				
1. REPORT DATE (DD-MM-YYYY)		2. REPORT TYPE		3. DATES COVERED (From - To)
		New Reprint		-
4. TITLE AND SUBTITLE			5a. CONTRACT NUMBER	
Multi-scale ballistic material modeling of cross-ply compliant composites			W911NF-09-1-0513	
			5b. GRANT NUMBER	
			5c. PROGRAM ELEMENT NUMBER	
			622105	
6. AUTHORS			5d. PROJECT NUMBER	
M. Grujic, G. Arakere, T. He, W.C. Bell, P.S. Glomski, B.A. Cheeseman				
			5e. TASK NUMBER	
			5f. WORK UNIT NUMBER	
7. PERFORMING ORGANIZATION NAMES AND ADDRESSES			8. PERFORMING ORGANIZATION REPORT NUMBER	
Clemson University Office of Sponsored Programs 300 Brackett Hall Clemson, SC 29634 -5702				
9. SPONSORING/MONITORING AGENCY NAME(S) AND ADDRESS(ES)			10. SPONSOR/MONITOR'S ACRONYM(S) ARO	
U.S. Army Research Office P.O. Box 12211 Research Triangle Park, NC 27709-2211			11. SPONSOR/MONITOR'S REPORT NUMBER(S)	
			56526-EG.3	
12. DISTRIBUTION AVAILABILITY STATEMENT				
Approved for public release; distribution is unlimited.				
13. SUPPLEMENTARY NOTES				
The views, opinions and/or findings contained in this report are those of the author(s) and should not be construed as an official Department of the Army position, policy or decision, unless so designated by other documentation.				
14. ABSTRACT				
The open-literature material properties for fiber and polymeric matrix, unit-cell microstructural characteristics, atomic-level simulations and unit-cell based finite-element analyses are all used to construct a new continuum-type ballistic material model for 0°/90° cross-ply highly-oriented polyethylene fiberbased armor-grade composite laminates. The material model is formulated in such a way that it can be readily implemented into commercial finite-element programs like ANSYS/Autodyn [ANSYS/Autodyn]				
15. SUBJECT TERMS				
Polymer-matrix composites (PMCs), Damage tolerance, Finite element analysis (FEA), Armor-grade composites				
16. SECURITY CLASSIFICATION OF:			17. LIMITATION OF ABSTRACT	15. NUMBER OF PAGES
a. REPORT	b. ABSTRACT	c. THIS PAGE	UU	19a. NAME OF RESPONSIBLE PERSON
UU	UU	UU	UU	Mica Grujic
				19b. TELEPHONE NUMBER
				864-656-5639

Report Title

Multi-scale ballistic material modeling of cross-plyed compliant composites

ABSTRACT

The open-literature material properties for fiber and polymeric matrix, unit-cell microstructural characteristics, atomic-level simulations and unit-cell based finite-element analyses are all used to construct a new continuum-type ballistic material model for 0°/90° cross-plyed highly-oriented polyethylene fiberbased armor-grade composite laminates. The material model is formulated in such a way that it can be readily implemented into commercial finite-element programs like ANSYS/Autodyn [ANSYS/Autodyn version 11.0, User Documentation, Century Dynamics Inc. a subsidiary of ANSYS Inc. (2007)] and ABAQUS/Explicit [ABAQUS version 6.7, User Documentation, Dessel Systems, 2007] as a User Material Subroutine. Model validation included a series of transient non-linear dynamics simulations of the transverse impact of armor-grade composite laminates with two types of projectiles, which are next compared with their experimental counterparts. This comparison revealed that a reasonably good agreement is obtained between the experimental and the computational analyses with respect to: (a) the composite laminates' capability, at different areal densities, to defeat the bullets with different impact velocities; (b) post-mortem spatial distribution of damage within the laminates; (c) the temporal evolution of composite armor laminate back-face bulging and delamination; and (d) the existence of three distinct penetration stages (i.e. an initial filament shearing/cutting dominated stage, an intermediate stage characterized by pronounced filament/matrix de-bonding/decohesion and the final stage associated with the extensive back-face delamination and bulging of the armor panel).

REPORT DOCUMENTATION PAGE (SF298)
(Continuation Sheet)

Continuation for Block 13

ARO Report Number 56526.3-EG

Multi-scale ballistic material modeling of cross-p ...

Block 13: Supplementary Note

© 2009 . Published in Composites Part B: Engineering, Vol. Ed. 0 40, (6) (2009), (, (6). DoD Components reserve a royalty-free, nonexclusive and irrevocable right to reproduce, publish, or otherwise use the work for Federal purposes, and to authorize others to do so (DODGARS §32.36). The views, opinions and/or findings contained in this report are those of the author(s) and should not be construed as an official Department of the Army position, policy or decision, unless so designated by other documentation.

Approved for public release; distribution is unlimited.



Multi-scale ballistic material modeling of cross-ply compliant composites

M. Grujicic^{a,*}, G. Arakere^a, T. He^a, W.C. Bell^a, P.S. Glomski^a, B.A. Cheeseman^b

^aInternational Center for Automotive Research CU-ICAR, Department of Mechanical Engineering, Clemson University, Clemson, SC 29634, United States

^bArmy Research Laboratory – Survivability Materials Branch, Aberdeen, Proving Ground, MD 21005-5069, United States

ARTICLE INFO

Article history:

Received 2 December 2008

Received in revised form 21 January 2009

Accepted 7 February 2009

Available online 7 May 2009

Keywords:

A. Polymer-matrix composites (PMCs)

B. Damage tolerance

C. Finite element analysis (FEA)

Armor-grade composites

ABSTRACT

The open-literature material properties for fiber and polymeric matrix, unit-cell microstructural characteristics, atomic-level simulations and unit-cell based finite-element analyses are all used to construct a new continuum-type ballistic material model for 0°/90° cross-ply highly-oriented polyethylene fiber-based armor-grade composite laminates. The material model is formulated in such a way that it can be readily implemented into commercial finite-element programs like ANSYS/Autodyn [ANSYS/Autodyn version 11.0, User Documentation, Century Dynamics Inc. a subsidiary of ANSYS Inc. (2007)] and ABAQUS/Explicit [ABAQUS version 6.7, User Documentation, Dassault Systems, 2007] as a User Material Subroutine. Model validation included a series of transient non-linear dynamics simulations of the transverse impact of armor-grade composite laminates with two types of projectiles, which are next compared with their experimental counterparts. This comparison revealed that a reasonably good agreement is obtained between the experimental and the computational analyses with respect to: (a) the composite laminates' capability, at different areal densities, to defeat the bullets with different impact velocities; (b) post-mortem spatial distribution of damage within the laminates; (c) the temporal evolution of composite armor laminate back-face bulging and delamination; and (d) the existence of three distinct penetration stages (i.e. an initial filament shearing/cutting dominated stage, an intermediate stage characterized by pronounced filament/matrix de-bonding/decohesion and the final stage associated with the extensive back-face delamination and bulging of the armor panel).

© 2009 Elsevier Ltd. All rights reserved.

1. Introduction

Fiber-reinforced polymer-matrix composites are among the most advanced commercially-available materials. While they are widely used in aerospace and defense-related industries, their application in construction, automotive and sporting-good industries is also quite common. The main reason for the aforementioned widespread use of the composite materials is their ability to simultaneously meet a variety of functional and manufacturing requirements. For example, the new Boeing 787 Dreamliner is primarily made of carbon-fiber-reinforced epoxy-matrix composites which, in addition to having outstanding mechanical properties, do not suffer from the similar manufacturing constraints as their metallic counterparts/alternatives, allowing a higher degree of optimization of the 787 aerodynamics. Furthermore, the composite airframes weigh less and are stronger than conventional airframes, which lead to improvements in the vehicle's operating efficiency and performance. Lastly, carbon-fiber-reinforced epoxy-matrix composites tend to resist corrosion and fatigue, the two phenomena which are well-established to cause gradual degradation and ultimate failure of metallic airframes.

The fiber-reinforced polymer-matrix composites like the one described above in which the main figures of merit are their density-normalized stiffness (i.e. *specific stiffness*) and density-normalized strength (i.e. *specific strength*) are commonly referred to as “*structural-grade*” composites. Many blast- and ballistic-protection systems in military and civilian applications are, on the other hand, made of another class of fiber-reinforced polymer-matrix composites, the so-called “*armor-grade*” composites [3,4]. The latter class of composites generally is optimized with respect to its ballistic-impact protection resistance, i.e. with respect to its energy absorbing capability. Consequently, the most commonly cited figures of merit in these materials are: (a) a critical level of the projectile's velocity or the projectile's kinetic energy (generally referred to as the “*ballistic limit*”) below which no full perforation takes place [5,6] and (b) an extent to which material ballistic-protection resistance is compromised in the material systems which are partially penetrated by projectile(s) or whose strike-face surface is damaged by the projectile(s).

The armor-grade composites are generally constructed using high specific-modulus/high specific-strength polymeric fibers such as aramid (e.g. Kevlar[®], Twaron[®], etc.) or oriented polyethylene fibers (e.g. Spectra[®], Dyneema[®], etc.) with an outstanding impact resistance [7–11]. The fibers, in the form of either woven fabrics or in the form of 0°/90° cross-ply collimated continuous

* Corresponding author. Tel.: +1 864 656 5639; fax: +1 864 656 4435.
E-mail address: mica.grujicic@ces.clemson.edu (M. Grujicic).

filaments, are embedded in the resin/polymer matrix. To attain maximum utilization of the inherently-high transverse-impact resistance of the fibers, the polymer-matrix content does not typically exceed 20% by volume. As a result of the very low resin content, these composites remain flexible/compliant to relatively high laminate thicknesses. Penetration resistance of the armor-grade composites is frequently increased through the use of hybrid structures in which a hard metallic or ceramic strike-plate is attached to the front of an armor-grade composite laminate.

Armor-grade composite laminates based on aramid fiber-reinforced phenolic-poly-vinyl-butyl resin and on 0°/90° cross-ply oriented polyethylene fiber-reinforced vinyl-ester are widely used in hard personnel-armor systems (e.g. protective helmets) for protection against fragments from exploding munitions [10–15]. These armor-grade composites are also increasingly being used for ballistic protection in light-weight armored vehicles, helicopters, patrol boats and transportable shelters (e.g. command shelters) [10]. Over the past decade, considerable efforts have been invested in carrying out various experimental investigations in order to identify and elucidate various penetration-failure mechanisms of the armor-grade fiber-reinforced composites under transverse impact loading and to compare and contrast these mechanisms with those operating in the related resin-free fabrics and resin-rich structural-grade composites. The main results obtained in these investigations can be summarized as follows [16–23]:

(a) In sharp contrast to the penetration of resin-free fabrics which is dominated by the successive fracture of individual yarns along the periphery of the penetrator head and by the side-way/lateral movement of the yarns which enables them to slip off from the penetrator, the penetration of armor-grade composites is mainly governed by the failure of principal yarns (the yarns which are in direct contact with the penetrator head). This observation is attributed to the effect of resin matrix on reducing yarn mobility which prevents them from slipping off from the penetrator. In general, stiffer resin matrices (e.g. vinyl-ester vs. polyurethane) tend to constrain the yarn movement to a greater degree and to force the penetrator to engage and fracture more yarns during penetration. This typically results in improved ballistic-protection resistance of armor-grade composites and is the reason that armor-grade composites reinforced with woven-yarn fabric are generally found to possess a higher energy-absorption potential than their resin-free fabric counterparts. However, excessive confinement of the yarns/filaments due to overly-high matrix stiffness and/or excessive amounts of the matrix may have a deleterious effect on the ballistic-protection performance of this class of composites. The latter effect is related to the fact that highly confined fibers are more likely to fail in transverse shear before experiencing any significant extensions in the longitudinal direction.

(b) Since the energy absorbed by the armor-grade composite is found to scale with the number of broken yarns in its fabric constituent, fiber tensile straining and ultimate fracture is believed to be the dominant mechanism for absorption of the projectile kinetic energy.

(c) In addition to fiber fracture, both woven-fabric-reinforced and cross-ply fiber-reinforced composite laminates are generally found to include additional complex failure processes such as: (i) delamination, (ii) a plug punch out, (iii) resin matrix cracking, and (iv) fiber pull-out. These failure modes are also typically observed in conventional structural-grade composites reinforced with glass or carbon fibers.

(d) In the case of multi-ply armor-grade composite laminates reinforced with either cross-ply collimated Spectra fibers or with woven Spectra fabrics, the following fracture modes are most often observed [1]: (i) sequential delamination, (ii) plug punch out induced by the through-the-thickness shear, and (iii) combined fiber

shearing/cutting and fiber tensile failure. In the cross-ply laminates, fibers in the top plies are typically found to fail by shearing/cutting, primarily along the edges of the projectile. Fibers located in the back layers of the laminates, on the other hand, generally fail in tension although in thin laminates, the lateral motion of fibers and/or fiber pull-out rather than fiber tensile straining to fracture is sometimes observed.

(e) The delamination in the cross-ply Spectra fiber-reinforced composite laminates is typically found to resemble the “generator strip” phenomenon [22] seen in glass fiber-reinforced epoxy-matrix structural-grade composites. That is, under transverse impact, the projectile pushes a strip of the first lamina toward the rear of the laminate which induces shear cracks in the resin matrix parallel to the fibers and applies a transverse load to the second lamina. This, in turn, causes separation between the first two laminae, i.e. delamination. After the aforementioned delamination process had taken place successively through the entire thickness of the laminate via the same mechanism and penetration of the laminate has occurred, narrow strips of damage zone remain visible under transmitted light and the strips are found to tend to follow the respective fiber orientation in the panel. These strips typically contain numerous matrix/fiber interface cracks. In addition, a circular delamination zone is generally seen around the perforation hole.

(f) In contrast to the case of cross-ply fiber-reinforced composite laminates, fabric-reinforced laminates are found to exhibit much less lateral movements of reinforcing fibers during the penetration of the projectile [3,4]. Even in thin panels, fibers apparently failed due to shearing/cutting in the laminae near the strike-face and in tension at the rear of the completely penetrated laminates. The presence of a narrow strip of the first lamina pushed forward by the penetrator is generally not observed. Instead, the delamination zones are observed preferentially along the two reinforcement directions of woven fabric. However, these damage zones are closely integrated with the circular delamination zone around the perforation hole. The occurrence of less anisotropic pattern of delamination was linked with the presence of resin-rich pockets between the reinforcing layers and with a greater constraint to matrix crack propagation parallel to the fibers/yarns.

(g) Up to the thickness of ~ 3 mm, the kinetic energy for full perforation of armor-grade composites has been found to depend on the laminate thickness in a way similar to that observed in ductile monolithic materials (e.g. poly-carbonate or aluminum).

The full-perforation kinetic energy vs. laminate thickness relationship, however, was found to be somewhat non-linear. This finding has been attributed to the unique mode of tensile failure seen in these materials for which the critical level of kinetic energy for full perforation is lowered by the fiber/yarn mobility.

The first use of fiber-based composites (primarily nylon (*polyamide*) fabric and *E-glass* fiber/ethyl cellulose composites) in body armor systems in place of the traditionally used metallic solutions can be traced back to the Korean War [24]. Although, primarily due to their low cost, nylon and *E-glass* fibers are still being used today, high-performance polymeric fibers are now the standard in most fiber-reinforced body-armor applications. The high-performance polymeric fibers used today are characterized by substantially improved strength, stiffness and energy-absorbing capacity. Among these high-performance fibers the most notable are: (a) *polyaramids* (e.g. Kevlar®, Twaron®, Technora®); (b) highly-oriented ultra high molecular weight *polyethylene*, UHMWPE (e.g. Spectra®, Dyneema®); (c) *poly-benzobis-oxazole*, PBO (e.g. Zylon®); and (d) *poly-pyridobisimidazole*, PIPD (e.g. M5®). When tested in tension, all these materials differ significantly from the nylon fibers, having very high absolute stiffness, extremely high specific strength, and quite low (<4%) strains-to-failure. These fibers essentially behave, in tension, as rate-independent linear elastic materials. When tested in transverse compression, however, these fibers are similar

to nylon and can undergo large plastic deformation without a significant loss in their tensile load-carrying capacity. This behavior is quite different from that found in carbon or glass fibers, which tend to shatter under transverse compression loading conditions.

The ballistic performance of high-performance polymeric fibers is, in general, quantified with respect to their ability to: (a) absorb the projectile's kinetic energy locally and (b) spread out the absorbed energy fast before local conditions for the failure are met. In simple terms, the ability of high-performance fibers to absorb energy per their unit mass, E_{sp} , is related to the fiber tenacity/failure strength, σ_{fail} , the fiber strain-to-failure, ϵ_{fail} , and the fiber density, ρ , as:

$$E_{sp} = 0.5\sigma_{fail}\epsilon_{fail}/\rho \quad (1)$$

The ability of fibers to spread out energy is governed by their speed of sound, v_{sound} , which is defined in terms of their axial modulus of elasticity, E , and their density, ρ , as:

$$v_{sound} = (E/\rho)^{(1/2)} \quad (2)$$

In Fig. 1, the two aforementioned ballistic performance parameters are displayed for the most-commonly used high-performance fibers. A summary of the key properties of the same set of high-performance fibers is provided in Table 1.

While the results displayed in Fig. 1 clearly reveal a high ballistic potential of the high-performance fibers in general (and specifically of the highly-oriented UHMWPE fibers, the type of fiber-reinforcements considered in the present work), full utilization of this potential in armor-grade composites turned out to be a formidable challenge because a number of additional factors (e.g. fabric/ply structure/architecture, ply areal density, fiber-to-fiber/yarn-to-yarn and fiber/yarn-to-projectile friction, type of polymeric matrix, composite processing and fabrication conditions, shape, mass and mechanical properties of the projectile to be defeated, etc.) become important. To overcome these challenges, the development of flexible-armor systems has started to rely increasingly more on the use of transient non-linear dynamics computational analyses of the ballistic response of armor when impacted with high-speed projectiles. For these analyses to yield reliable predictions and for them to be used as complements to the accompanying experimental investigations, high-fidelity physically-based material models for the armor-grade composite materials must be available.

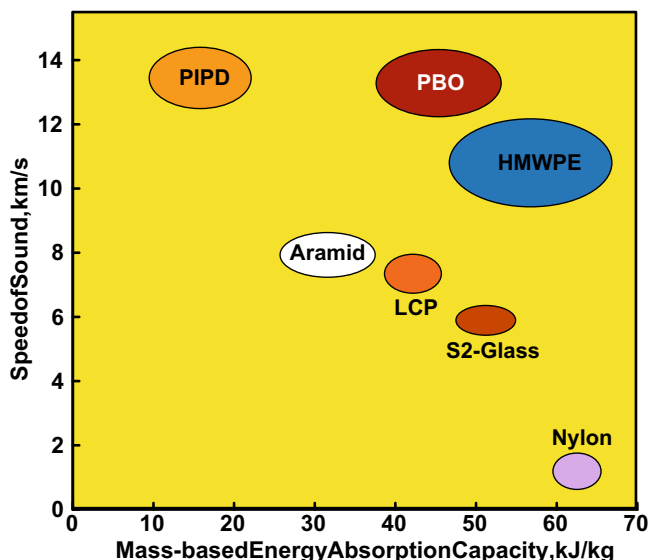


Fig. 1. Sound speed vs. mass-based energy absorption capacity for a number of high-performance fibers.

A review of the public-domain literature carried out as part of the present work revealed the existence of several material models for armor-grade composites [25–30]. While such models have provided an important insight into the roles of a number of factors mentioned above, they suffer from three major shortcomings: (a) some are more phenomenological, i.e. less physically-based in their character; (b) others require the knowledge of a relatively large number of parameters; and (c) may not very efficient computationally. In addition to the models mentioned above, purely phenomenological models [e.g. 31] also exist in the literature. Such models are the result of extensive experimental efforts and typically have, within the same family of armor-grade composite materials, a high practical utility. However, they provide no insight into the complicated physics of projectile/armor interactions and can not be used across the boundaries of different armor-type composite families.

To overcome the aforementioned limitations of the two groups of material models, a new multi-scale physically-based computationally-efficient material model for UHMWPE-filament (e.g. Spectra[®], Dyneema[®], etc.) based armor-grade composites is developed, parameterized and validated in the present work. A preliminary version of this model without details regarding the atomic-level analysis of the filament/matrix interfacial bonding/de-bonding and without detailed validation was previously reported Grujicic et al. [32]. Since it is generally-established that for the UHMWPE fiber-based armor-grade composites, a substantially higher ballistic-protection performance is obtained when such fibers are used as 0°/90° cross-ply layers of highly-oriented filaments rather than woven fabrics, only the former composite-laminate architecture will be addressed in the present work. In passing, it should be mentioned that it is believed that the deflection of stress waves at the yarn/yarn or fiber/fiber cross-ever points in woven fabric (the process which lowers the ability of fibers to spread out energy along their axis) is the main reason for their inferior ballistic performance.

As stated above, the main objective of the present work was to develop, parameterize and validate, (against the relevant experimental results), a simple physically-based computationally-efficient continuum-level material model for a prototypical 0°/90° cross-ply oriented polyethylene fiber-based armor-grade composite material. While developing this model, unit-cell level finite-element analyses of the meso-scale material mechanical response and properties and atomic-level simulations of the filament/matrix bonding/de-bonding had to be employed giving the present approach a multi-length scale character.

It should be noted that within a fully multi-scale computational approach, the underlying boundary-value problem is set-up and simultaneously solved at several length scales (e.g. at atomistic,

Table 1
Typical mechanical properties of high-performance fibers.

Fiber type	Failure strength (GPa)	Failure strain	Axial modulus (GPa)	Density (kg/m ³)
Aramid	2.8–3.2	0.015–0.045	60–115	1390–1440
HMWPE	2.8–4.0	0.029–0.038	90–140	970–980
LCP	2.7–2.9	0.033–0.035	64–66	1400–1420
PBO	5.4–5.6	0.024–0.026	270–290	1540–1560
PIPD	3.9–4.1	0.011–0.013	320–340	1690–1710
Nylon	0.06–0.08	1.5–2.5	1.0–1.5	1070–1170
S-glass	4.64–4.66	0.053–0.055	82–92	2470–2490

meso, macro). This approach will be adopted in our future work. In the present investigations, a simpler, and computationally more efficient yet less accurate approach was adopted. That is, results from the experimental investigation of Iremonger [36] are used to infer the main deformation and fracture mechanisms of the composite material under investigation and a coupled meso-scale/continuum level model is constructed. However, critical filament/matrix de-bonding parameters needed in this model were determined in a separate atomic level computational investigation, described in Appendix A.

The organization of the paper is as follows: Details regarding the computational procedures employed to develop a new unit-cell continuum-damage based material model for a prototypical 0°/90° cross-plyed uni-directional UHMWPE-filament based armor-grade composite and the implementation of this model into a material user subroutine suitable for use in commercial finite-element programs are presented in Section 2. The formulation of a simple projectile-target impact problem used to validate the new material model is described in Section 3. Main results obtained in the current work are presented and discussed in Section 4. The main summary points and conclusions resulting from the present work are listed in Section 5. A brief discussion regarding the atomic-scale computational analysis used to investigate filament/matrix bonding/de-bonding behavior is presented in Appendix A.

2. Material model formulation and implementation

In this section and its subsections, a detailed account is given of the procedure used to develop a new unit-cell continuum-damage

based multi-scale material model for a prototypical single-lamina 0°/90° cross-plyed uni-directional UHMWPE-filament based armor-grade composite. Also details regarding the implementation of the model into a material-user subroutine suitable for use in commercial finite-element packages are presented. The basic idea behind the unit-cell based approach is that the mechanical response of the unit-cell (consisting of high-stiffness/high-strength polymeric filament segments and a compliant polymeric matrix) can be smeared out (homogenized) into an equivalent response of a (anisotropic) continuum material. A simple schematic of the unit cell which is used to represent 0°/90° cross-plyed unidirectional UHMWPE-filament based armor-grade composites allotted to a single filament crossover is depicted in Fig. 2(a). Its continuum-level material point counterpart is represented in Fig. 2(b). Within the continuum-material framework, filaments are not represented explicitly but rather by two material directions whose orientations are denoted in terms of material vectors, g_1 and g_2 . (Please note that vectors are denoted using a bold lower-case font, tensors using a bold upper-case font while scalars using a non-bold font.) The “unit-cell” term is used to denote the basic structural block so that a piece of the armor-grade composite material can

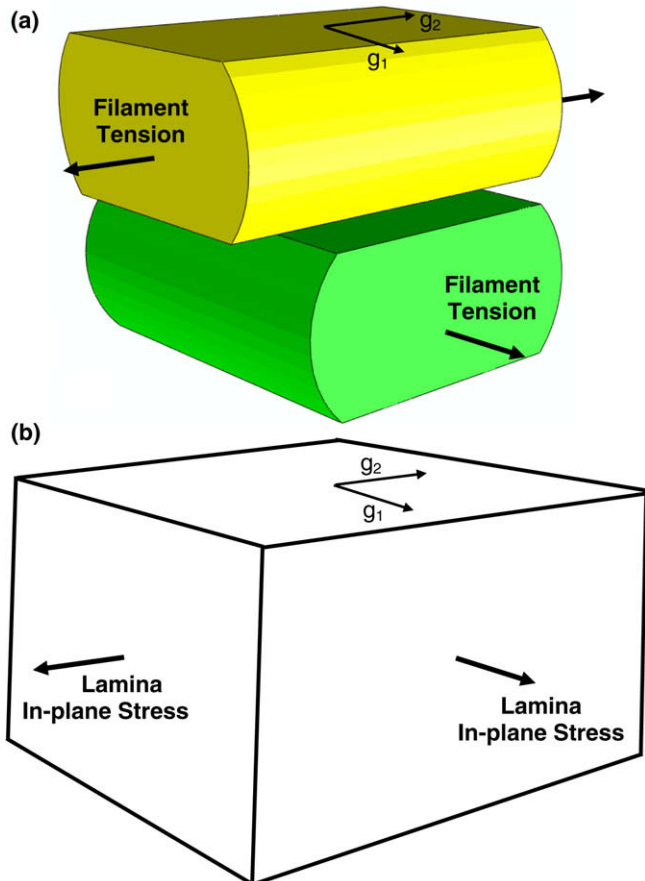


Fig. 2. The relationship between a unit cell and the corresponding material point in an anisotropic continuum.

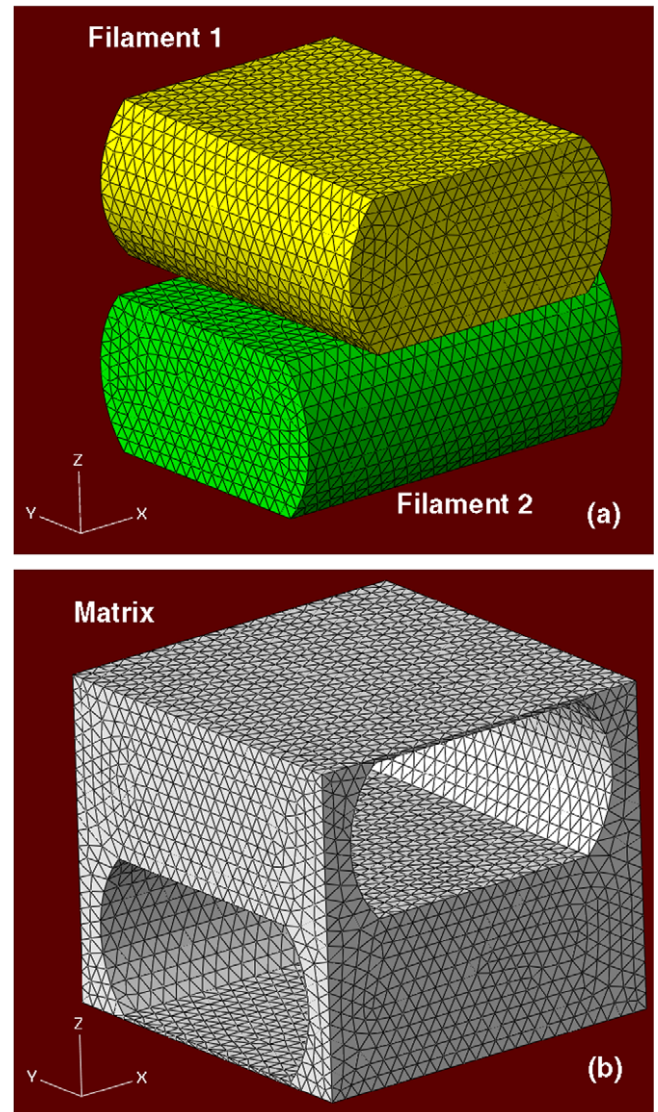


Fig. 3. Typical finite-element meshes used in the unit-cell computational analyses to discretize: (a) the two filaments and (b) the matrix.

Table 2
The orthotropic linear elastic material data for UHMWPE filaments [31].

E_{11} (GPa)	E_{22} (GPa)	E_{33} (GPa)	G_{12} (GPa)	G_{13} (GPa)	G_{23} (GPa)	ν_{12}	ν_{13}	ν_{23}
118.0	6.0	6.0	6.0	6.0	6.0	0.3	0.3	0.4

Axial failure strain = 0.05; transverse shear strength = 350 MPa.

be considered as a result of the repetition of this block in three orthogonal directions.

Coupling between the continuum material formulation and the unit-cell geometry and mechanical response is done in the following way: (a) the deformation state of a continuum material point (as quantified by the corresponding deformation gradient) is used to update the unit-cell geometry; (b) the updated unit-cell geometry and the state of the continuum material at the end of the previous time increment are used to update the extent of structural damage in the unit cell; and (c) the updated material state obtained in point (b) is then used to compute the stress state at the end of the current time increment.

It must be recognized that in order for the aforementioned approach to be valid (i.e. in order for homogenization of the armor-grade composite unit-cell response to be justified), the characteristic lengths in the numerical analysis in which the model is used (e.g. the projectile and the target dimensions in a projectile/target impact problem analyzed in the present work and the associated stress/strain gradient ranges) must be large in comparison to the unit-cell edge lengths. In most practical situations, this appears to be the case since the unit cell edge length is in the range between 10 and 30 μm .

2.1. Meso-scale unit-cell level finite-element analyses

The salient feature of the proposed computational approach is that the mechanical response of a continuum-level material point (corresponding to a unit cell in the armor-grade composite) and the accompanying changes in constituent materials (primarily those associated with the filament/matrix interfacial de-bonding) can be inferred by carrying out a series of meso-scale finite-element analyses pertaining to relatively simple mechanical tests of the unit cell. In these analyses, a detailed representation of the unit-cell microstructure is considered. In this section, details are presented regarding the geometrical models used in the construction of the unit cell, material properties/models assigned to the filament segments, matrix and the filament/matrix interfacial bonding/de-bonding, and the finite-element analyses used to determine the mechanical response and the material evolution under different loading conditions. As will also be shown in this section, to obtain quantitative information about the filament/matrix interfacial bonding/de-bonding, atomic-level simulations were employed. This portion of the work is covered in more details in Appendix A. It should be noted that, as correctly pointed out by one of the reviewers of the present work, interfacial de-bonding parameters can be also measured experimentally using one of the methods such as the so-called “fiber push-out” method.

Table 3
Normal and shear filament/matrix de-bonding parameters used in the present work.

Normal de-bonding			Shear de-bonding		
Initiation displacement–discontinuity (μm)	Bond strength (MPa)	Complete de-bonding displacement–discontinuity (μm)	Initiation displacement–discontinuity (μm)	Bond strength (MPa)	Complete de-bonding displacement–discontinuity (μm)
0.05	18.0	1.1	0.9	23.0	2.1

An example of the finite-element meshes used in the unit-cell computational analyses is displayed in Fig. 3(a) and (b). 20,847 first order tetrahedron elements (ABAQUS/Explicit designation C3D4) are used to discretize each of the two filament segments, Fig. 3(a), while 21,606 elements of the same type are used to discretize the matrix, Fig. 3(b). Bonding between the matrix and the filaments is represented using 7056 “cohesive” elements, (ABAQUS/Explicit designation COH3D6).

The polymeric filaments (assumed to be based on the UHMWPE) are modeled as orthotropic (more precisely as planar isotropic) linear elastic materials (up to the point of failure under axial tension or transverse shear) with the unique material direction being aligned with the filament axis. A summary of the elastic and failure properties of the filament material is provided in Table 2.

The polymeric matrix (assumed to be based on styrene–isoprene–styrene tri-block copolymer [33]) is modeled, due to attendant high-deformation rate conditions, as a linear isotropic material with a Young’s modulus of 3 GPa and a Poisson’s ratio of 0.4.

Bonding between the filaments and the matrix is modeled using traction vs. interfacial displacement–discontinuity relations (one for the normal and one for the tangential displacements). These two relations are characterized by a linear traction vs. displacement/discontinuity relation unto the point of damage initiation and with a linear “Downhill” post damage relationship. Consequently the two modes “Normal and Shear” of interfacial-bonding damage are each characterized by three parameters: (a) critical normal or shear interfacial-displacement discontinuities at which damage initiation begins; (b) the corresponding normal or shear interfacial strengths; and (c) normal or shear interfacial-displacement discontinuities at which complete filament/matrix decohesion takes place. A summary of the interfacial cohesion parameters used in the present work is given in Table 3. These parameters were determined in a separate molecular-statics based investigation of atomic-level mechanical properties of the composite materials consisting of the unidirectional UHMWPE filaments and an amorphous polymeric matrix. Few details regarding the atomic-level analysis carried out and the results obtained are presented in Appendix A. The procedure used closely follows that presented in our recent work [34] in which atomic level properties of composite materials consisting of multi-walled carbon nanotube reinforcements and a poly-vinyl-ester-epoxy matrix were investigated.

Interactions between the filaments and the matrix after decohesion are accounted for through a “Hard” pressure vs. over closure algorithm within which the interacting bodies must be in contact before they can interact and the pressure levels that can be transmitted through the contact interactions are unbounded. Relative sliding of the contacting bodies is opposed by a frictional force based on a constant friction coefficient.

The following simple mechanical tests were carried out using the meso-scale unit-cell based finite-element approach described above: (a) uniaxial tension along the axis of one of the filaments (i.e. along the directions 1 or 2); (b) uniaxial tension in a direction normal to the single-lamina surface (direction 3); (c) in-plane 1–2 shear; and (d) the transverse shear.

It is well-established that the presence of free surfaces (along which loading is applied) in isolated unit cells, like the one used in the present work, can alter the unit cell mechanical response relative to the one displayed by “bulk” unit cells subjected to the same mode of loading. To provide the first-order assessment of these effects, few mechanical-test simulations were carried out using a block of $3 \times 3 \times 3 = 27$ unit cells. The results obtained show that the “surface-loading effects” can be significant. However, these effects were not included in the current rendition of the material model since this would have required the level of effort not available in the present work.

For each of the aforementioned tests, a series of loading–unloading–reloading cycles was applied in order to detect the onset of interfacial de-bonding and the resulting degradation in the corresponding continuum–material stiffness parameters. To determine how one mode of loading may affect all the unit-cell stiffness parameters, loading is done in one mode while subsequent reloading is done in all the modes (one at a time). It should be noted that simulations of the mechanical test mentioned above were done under loading rates comparable to those typically encountered in the bullet/target impact problems. Consequently, the inertial effects were accounted for, at least to the first order of approximation.

The results obtained suggest that interfacial de-bonding is mainly caused by the through-the-thickness tension (in direction 3) and by the in-plane shear (1–2 shear) and that E_{33} , G_{12} , G_{23} and G_{31} are mostly degraded by interfacial de-bonding. In addition, these four stiffness parameters are found to degrade essentially linearly with the extent of interfacial-bonding damage, D .

In accordance with the aforementioned observations and the atomic-level interfacial de-bonding initiation parameters listed in Table 3, the following strain-based damage initiation criterion was derived:

$$\left(\frac{\epsilon_{33}}{\epsilon_{33,init}}\right)^2 + \left(\frac{\gamma_{12}}{\gamma_{12,init}}\right)^2 = 1 \tag{3}$$

where $\epsilon_{33,init}$ and $\gamma_{12,init}$ are pure normal and shear strains at which damage initiation is first observed. In a $\frac{\epsilon_{33}}{\epsilon_{33,init}}$ vs. $\frac{\gamma_{12}}{\gamma_{12,init}}$ plot, Eq. (3) defines a unit (failure-initiation) circle. Within the same plane, the condition at which complete damage-induced degradation takes place is defined by an ellipse in the form:

$$\left(\frac{\epsilon_{33}}{\epsilon_{33,fail}}\right)^2 + \left(\frac{\gamma_{12}}{\gamma_{12,fail}}\right)^2 = 1 \tag{4}$$

where $\epsilon_{33,fail}$ and $\gamma_{12,fail}$ are pure normal and shear strains at which complete degradation ($D = 1$) takes place.

When the $(\epsilon_{33}, \gamma_{12})$ strain state of a material point (e.g. point B in Fig. 4) lies between the damage initiation circle and the failure ellipse, the corresponding extent of material damage is defined as the ratio of line segments AB and AC indicated in Fig. 4. The four continuum level damage parameters $\epsilon_{33,init}$, $\epsilon_{33,fail}$, $\gamma_{12,init}$ and $\gamma_{12,fail}$ are determined using the unit-cell finite-element analyses described in this section. The values of these four parameters are: 0.01, 0.04, 0.01 and 0.04, respectively.

It should be noted that, as correctly pointed out by one of the reviewers of the present work, the mechanical response (including the failure behavior) of composite materials is loading-rate dependent. Since the present material model is intended to be used only in the high loading-rate regime (the regime which dominates bullet/target interaction conditions), under which the constituent materials tend to behave essentially as linear elastic with weak rate dependency, the material model parameters utilized in the present work are treated as rate independent. Consequently, the

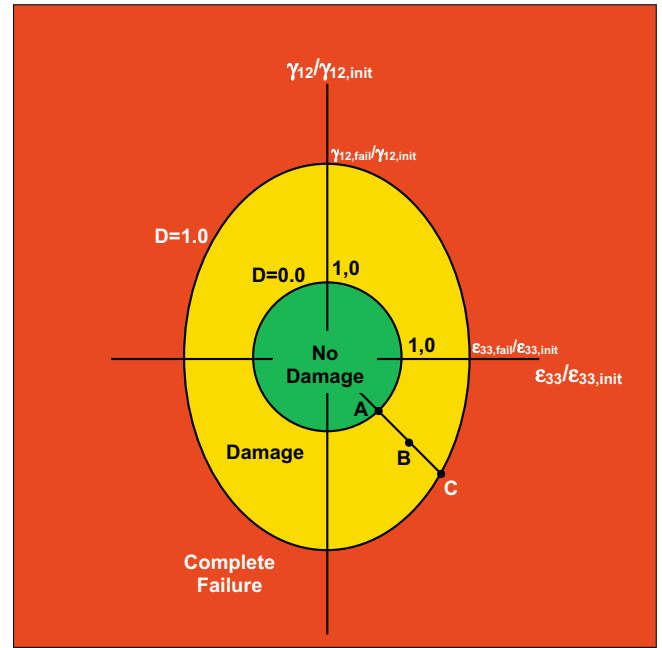


Fig. 4. A schematic of the computational procedure used to determine the onset and track the progress of material damage (interfacial de-bonding) within the unit cell.

present model is not suitable for use in the calculations dealing with low loading-rate structural response of these materials.

2.2. Determination of the unit-cell current geometry and architecture

As discussed earlier, a critical step in the development of the present continuum-damage material model is establishment of the relationship between the continuum-level material-point deformation state and the meso-scale unit-cell geometry. This topic is covered in the present section.

In general six independent geometrical parameters are needed to fully describe the current geometry of the unit cell. These parameters include: (a) The three unit-cell edge lengths, a_i ($i = 1-3$); (b) the in-plane shear inter-filament included angle, θ ; and (c) the two out-of-plane shear angles, ϕ and ψ . In this section it is shown how these parameters are related to the continuum-level deformation state of the material point corresponding to the unit cell in question.

At the continuum level, the state of deformation at a given material point is described by the deformation gradient, F , whose components in a Cartesian coordinate system are defined in Eq. (5) in Ref. [32]: Next, also at the continuum level, the 0° and 90° filaments can be described using vectors a_i ($i = 1, 2$) aligned with

Table 4

Experimental [36] and the corresponding computational [Present Work] results pertaining to the success of armor-grade composite test panel to stop a M855 bullet at different initial bullet velocities.

Test-panel thickness (mm)	Areal density (kg/m ²)	Bullet velocity (m/s)			
		600	700	800	900
4.2	4	–	–	–	G/G
11	10.5	G/G	G/G	G/G	G/G
15	13.7	–	O/O	O/O	G/G
22	21	U/U	U/U	U/U	U/U
32	31	U/U	U/U	U/U	U/U

Nomenclature: U – undermatched, O – overMatched, G – grossly overmatched; Experiment/Computation.

the axis of these filaments and the length of these vectors can be set equal to the corresponding current in-plane unit-cell edge lengths, a_i ($i = 1, 2$). These vectors and the vector a_3 which is aligned with the out-of-plane unit-cell edge can be related to their initial counterparts, $a_{i,0}$ ($i = 1-3$) as defined in Eq. (6) in Ref. [32]. The length of each a_i ($i = 1-3$) can be defined using Eq. (7) in Ref. [32] while the inter-filament included angle θ can be computed using Eq. (7) in Ref. [32]: An equation analogous to Eq. (8) in Ref. [32] can next be used to define the out-of-plane shear angles ϕ and ψ . Eqs. (5)–(8) in Ref. [32] can be used to show that the current geometry of the unit cell can be determined using the original unit-cell edge lengths and the current value of the deformation gradient.

Once the current unit-cell parameters are defined, standard relations are invoked to compute the corresponding normal and shear strains. Next, through-the-thickness normal strain ϵ_{33} and the in-plane shear strain γ_{12} and the procedure outlined in the previous section are used to update the extent of material damage and the affected stiffness moduli. It should be noted that material damage is irreversible, i.e. D cannot decrease during the deformation history of a material point.

2.3. Determination of the continuum material-point stress state

Once the extent of material damage is updated then E_{33} , G_{12} , G_{23} and G_{31} are degraded by multiplying their initial values by a factor $(1.0-cD)$, where $0.0 \leq c \leq 1.0$ is an elastic-modulus dependent parameter. Since the continuum material is modeled as a linear elastic orthotropic material with degradable stiffness moduli, the standard relationships are used to compute the stress components from the updated strain components and the updated material stiffness matrix.

Once the stresses are updated, the occurrence of filament failure is investigated. Filaments are allowed to fail in one of the two following modes: (a) in tension, when the tensile-strain/tensile-stress reaches a critical value or (b) due to transverse shear, when the corresponding transverse shear stress reaches a critical value. When either of these two filament failure modes takes place, the corresponding in-plane normal stress(es) and the corresponding transverse shear stress are set to a small residual value associated with the remaining matrix ligaments. Once the stresses are updated to include the effect of filament failure they are ready to be returned to the finite-element solver for the computation of the global equilibrium.

The present material model is, thus, constructed in such a way so that it can account for the competition between the following two processes: (a) Transverse-shear loading which is promoted

by good filament/matrix bonding and higher matrix stiffness. If sufficiently high transverse shear stresses are developed they can cause shear/type failure of the filament(s). In this case, the energy absorbed by the filaments is relatively small and, consequently, ballistic/protection performance of the armor-grade composite laminate is inferior and (b) stretching of the filaments till the point of failure. This process is promoted by filament/matrix de-bonding which enables the filaments to deform independently of the matrix. In this case, the energy absorbed by the filaments is maximum and the ballistic/protection of the armor is greatly enhanced. It should be noted that some critical level of filament-matrix bonding is needed to ensure that the filaments are not simply pushed laterally by advancing projectile which can lead to the defeat of the armor by the projectile via the so-called “Wedge Through Effect” [35].

2.4. Continuum material model implementation in a user-material subroutine

The unit-cell based material model described in the previous section is next implemented in the material user subroutine, VUMAT, of the commercial finite-element program ABAQUS/Explicit [2]. This subroutine is compiled and linked with the finite-element solver and enables ABAQUS/Explicit to obtain the needed information regarding the state of the material and the material mechanical response during each time step, for each integration point of each element. In the present work, first-order six-node general-purpose reduced-integration solid elements (ABAQUS/Explicit designation C3D6R) are used.

The essential features of the coupling between the ABAQUS/Explicit finite-element solver and the VUMAT Material User Subroutine at each time increment at each integration point of each element can be summarized as follows:

(a) The corresponding previous time-increment stresses and material state variables as well as the current time-step deformation gradient are provided by the ABAQUS/Explicit finite-element solver to the material subroutine. In the present work, the strain components, two variables pertaining to the not-failed/failed status of the filaments and one variable pertaining to the deletion status of the finite element are used as the state variables.

(b) Using the information provided in (a), and the unit-cell based material model presented in the previous section, the material stress state as well as values of the material state variable(s) at the end of the time increment are determined within the VUMAT and returned to the ABAQUS/Explicit finite-element solver. In addition, the changes in the total internal and the inelastic energies (where appropriate) are computed and returned to the solver.

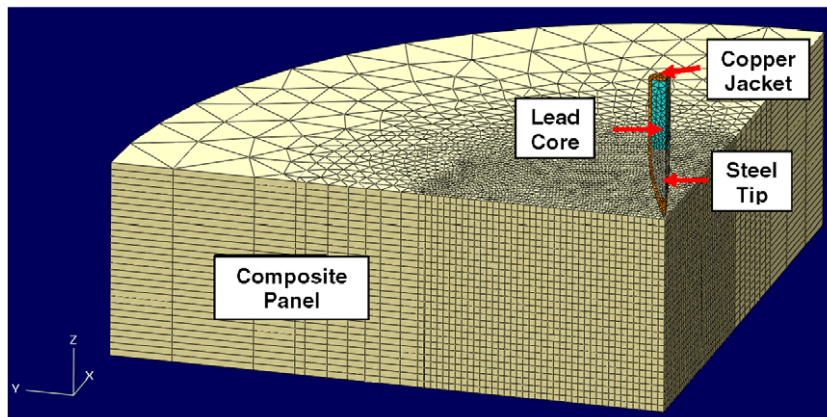


Fig. 5. Typical final element meshes used in the transient non-linear finite-element analyses of the impact of a full-jacketed metal bullet impact onto an armor-grade composite test panel. Due to inherit symmetry of the problem only one-quarter of the model is analyzed.

3. Validation of the material model

As stated earlier, the main objective of the present work was to develop a micro-structure-dependent physically-based material model for the armor-grade composites based on $0^\circ/90^\circ$ cross-plyed unidirectional UHMWPE filaments and a low-content (<20 mass%) polymeric matrix. In this section, a simple projectile/armor impact problem is described. The problem is used to carry out preliminary

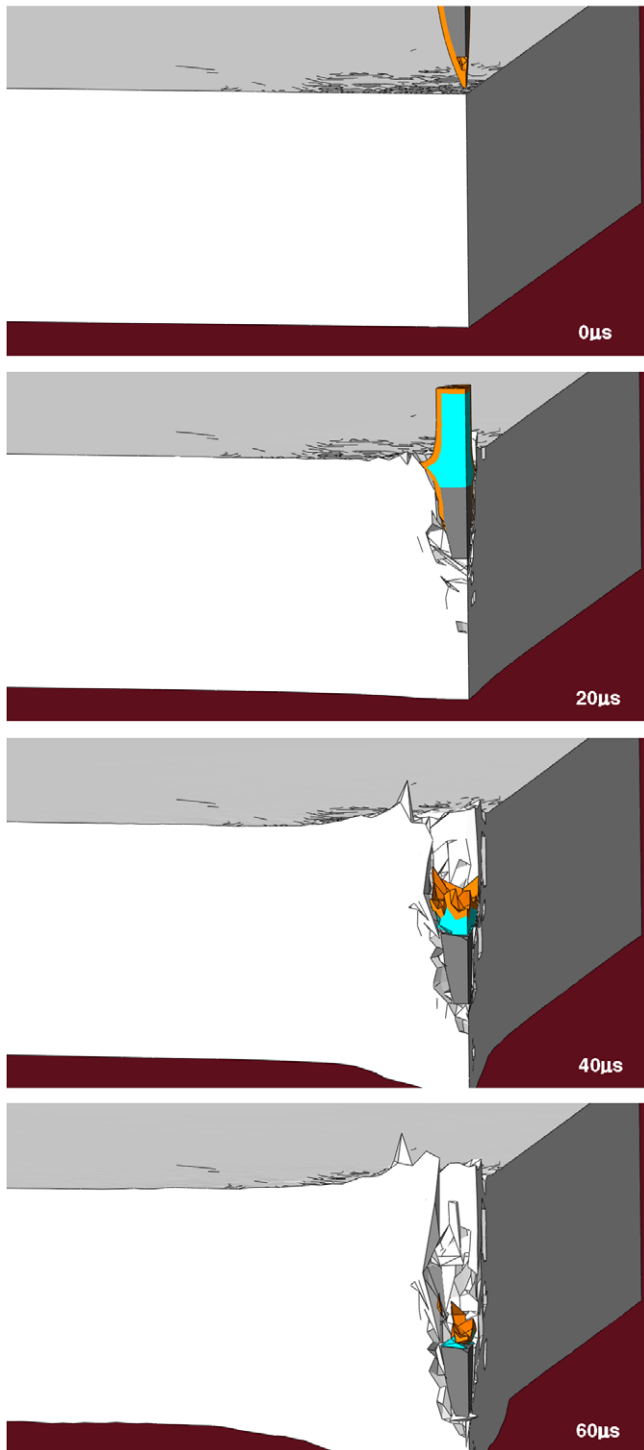


Fig. 6. An example of the temporal evaluation of the materials within the 22 mm-thick armor laminate and the M855 projectile. The initial projectile velocity equals 800 m/s.

testing and validation of the proposed unit-cell continuum-damage based material model against the previously reported experimental results of Iremonger [36] who impacted five different thickness (4.2 mm, 11 mm, 15 mm, 22 mm and 32 mm with areal densities given in Table 4) UHMWPE panels with two types of projectiles. Iremonger [36] fired two different 5.56 mm NATO projectiles, the M193 lead cored projectile with a gilding metal jacket and the M855, which is similar to the M193 but contains a hardened steel tip attached to the lead core. The approximate masses of the M193 and M855 projectiles are 3.5 g and 4.0 g, respectively. For the present computational investigation, the panels were simulated having a circular/disk shape with a radius of 90 mm.

An example of the initial configuration of the projectile/armor finite-element system analyzed here is shown in Fig. 5. Due to the inherent symmetry of the problem, only one-quarter of the model is analyzed and the appropriate symmetry boundary conditions are applied along the planes of symmetry. Typically (one-quarter of) the projectile is discretized in terms of 1955 first-order tetrahedron elements C3D4, while (one-quarter of) the composite panel is discretized using 382 first-order six-node brick elements, C3D6, per 1.1 mm-thick lamina. To reduce the computational burden, the size of the C3D6 elements is chosen to match that of the C3D4 elements only in the region of the composite panel impacted and greatly affected by the bullet. A coarser mesh was used in the section of the composite less affected by the bullet impact.

The three metallic materials (steel, lead and copper) present in the two types of bullets are modeled using (a linear equation of state, the Johnson–Cook strength model, the Johnson–Cook failure model and an erosion algorithm based on the maximum allowable instantaneous geometrical strain). Considering the fact that these material models were reviewed in our recent work [37], they will not be discussed any further here. The panel was assigned the material model developed in the present work.

To define the initial-conditions, zero initial velocities were assigned to all the nodes of the composite panel while a constant velocity in the negative Z direction was assigned to all the nodes of the bullet. Four initial projectile velocities were considered: 600 m/s, 700 m/s, 800 m/s and 900 m/s. To mimic the effect of clamping along the armor edges, fixed boundary conditions are applied to all the peripheral nodes of the composite panel.

The same hard interaction algorithm as that used in Section 2.1 was also employed to model interactions between the bullet and the target. To account for the sliding-friction resistance between the bullet and the target, a simple Coulomb friction model was used.

Computational analyses were run on a machine with two 2.33 GHz Quad-core Intel Xeon processors with 16GB of RAM. A typical run involving the 11 mm thick composite panel took ~12 min while in the case of a 32 mm-thick panel the wall-clock computational time was ~45 min.

4. Presentation of the results and discussion

As discussed earlier, the unit-cell continuum-damage material model for $0^\circ/90^\circ$ cross-ply UHMWPE filament based armor-grade composites is validated by comparing the computational results obtained in a series of transient non-linear dynamics finite-element analyses discussed in Section 3 with their experimental counterparts obtained in the work of Iremonger [36]. Iremonger [36] investigated five armor panels with a thickness from 4.2 mm to 32 mm, used two types of bullets (M855 and M193) and four initial velocities. Thus the full-factorial test matrix involves $5 \times 2 \times 4 = 40$ experiments. Not all 40 experiments were conducted in the work of Iremonger [36] and only selected results were reported for the experiments that were carried out. Three

types of results were reported: (a) the success of panel in stopping the bullet. Iremonger [36] used the following nomenclature: *undermatched* (to denote the cases when the panel was successful in stopping the projectile), *overmatched* (to denote the cases when the panel was fully penetrated by the bullet but was able to absorb a substantial amount of the bullets kinetic energy), and *grossly overmatched* (to denote the cases when the bullet was able to fully penetrate the panel by punching out a circular-disk shaped plug of the panel material without a significant loss in the bullets kinetic energy); (b) post-mortem micrographs of the vertical cut sections of the armor panel passing through the axis of the penetration hole; and (c) temporal-evolution plots of the back-face bulge height and the bulge diameter of the impacted panel. In the remainder of this section, a comparison is made between the computational and the experimental results for each of these three types of results.

An example of the typical computational results pertaining to the temporal evolution of materials in the armor-laminate and in the projectiles is shown in Fig. 6.

4.1. The success of armor test panels in stopping the bullet

The success of different composite panels in stopping the M855 bullet at different bullet velocities as determined experimentally by Iremonger [36] and computationally in the present work as dis-

played in Table 4. It is seen that the overall agreement between the two sets of results is quite reasonable suggesting that the proposed unit-cell continuum-damage based material model for cross-plyed UHMWPE filament based armor-grade composites is capable of capturing the essential features of the mechanical behavior of this material under ballistic loading conditions. Results analogous to those displayed in Table 4 were not reported in [36] for the M193 projectile; hence a similar experiment/computation comparison cannot be made for this type of projectile.

4.2. The mode, the extent and the spatial distribution of damage

In Ref. [36], three micrographs of the vertical cut sections of the composite panel (each passing through the axis of the penetration hole) were provided. Due to copyright restrictions, only schematics of these micrographs are included in the present work. The three micrographs correspond to the following panel/bullet/test conditions. (a) 11 mm thick test panel/M855/600 m/s, Fig. 7(a); (b) 22 mm thick test panel/M855/800 m/s, Fig. 8(a); (c) 22 mm thick test panel/M193/800 m/s, Fig. 9(a). The corresponding computational counterparts revealing the spatial distribution of damage in the armor panel obtained in the present work are displayed in Figs. 7–9(b), respectively.

A comparison of the results displayed in Figs. 7–9(a) with the ones displayed in Figs. 7–9(b), respectively, reveals that the overall

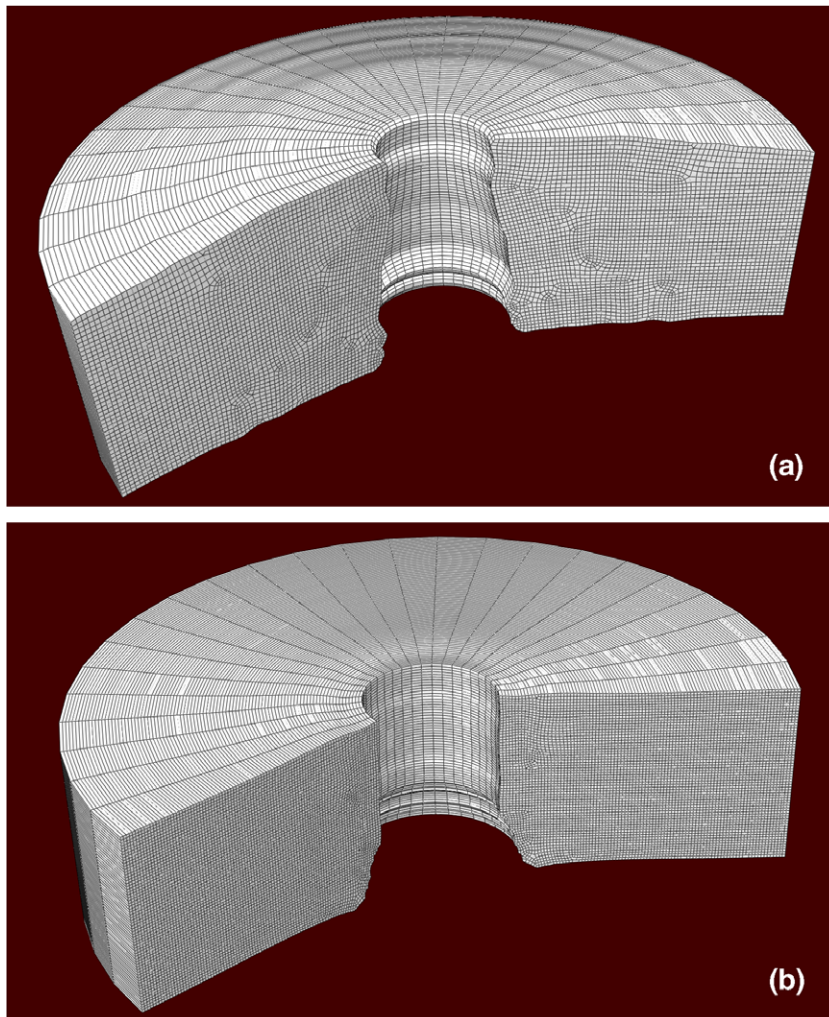


Fig. 7. A comparison between (a schematic of) the experimental results obtained in Ref. [36] (a), and their computational counterparts obtained in the present work (b), pertaining to the spatial distribution of damage in case of a M855 bullet initially propelled at a velocity of 600 m/s impacting an 11 mm thick test panel.

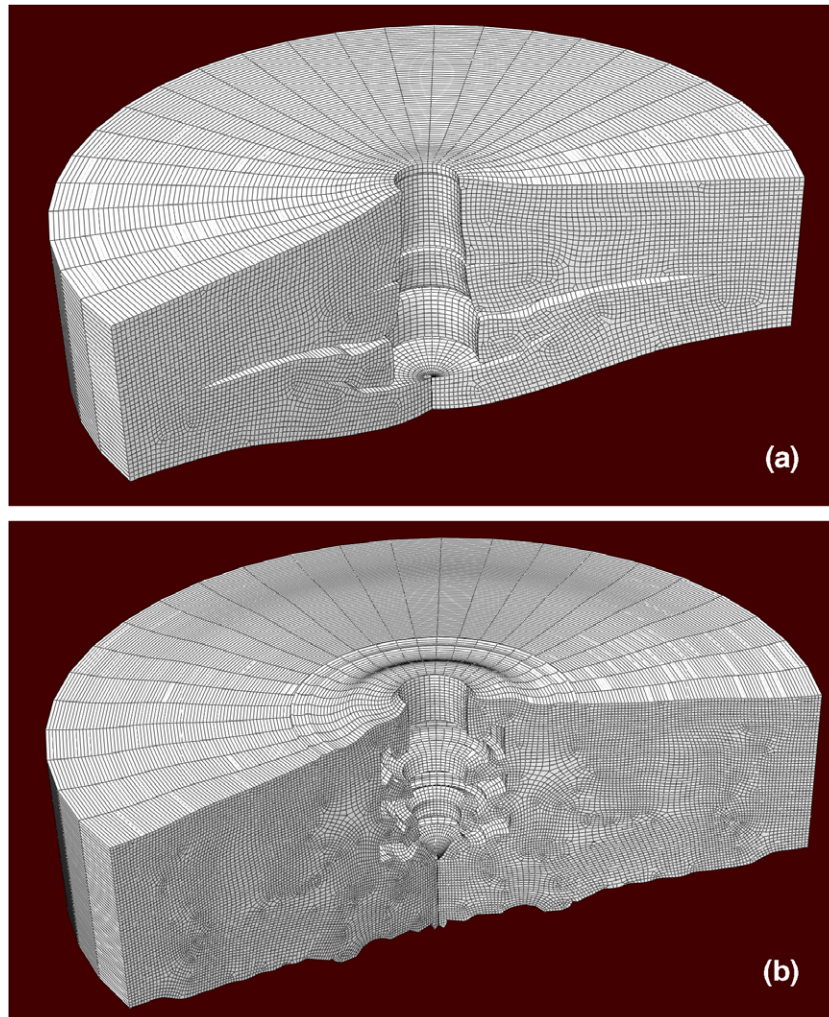


Fig. 8. A comparison between (a schematic of) the experimental results obtained in Ref. [36] (a), and their computational counterparts obtained in the present work (b), pertaining to the spatial distribution of damage in case of a M855 bullet initially propelled at a velocity of 800 m/s impacting a 22 mm thick test panel.

agreement between the two sets of results is reasonable. More specifically:

(a) In the case of 11 mm-thick composite panel impacted by an M855 projectile at an initial velocity of 600 m/s, both the experiment, Fig. 7(a), and the numerical results, Fig. 7(b), show a “Punch through” mode of penetration which is dominated by transverse shearing/cutting of the filaments and associated with relatively low absorption of the projectiles kinetic energy. In addition, the size of penetration hole and its changes through the armor-panel thickness are reasonably well reproduced by the present material model, Fig. 7(a) and (b).

(b) In the case of a 22 mm-thick composite panel impacted by an M855 projectile at an initial velocity of 800 m/s, both the experiment, and the numerical results show only a partial penetration (Fig. 8(a) and (b)). In the same figures it is seen that the depth of the penetration hole is somewhat under predicted by the computational analyses. On the other hand, both the experiment and the computational analysis predict that initial penetration of the composite panel is first dominated by filament shearing/cutting and subsequently by filament/matrix de-bonding/delamination. It should be noted that the present material model is based on the use of a homogenization technique which yields an equivalent single-phase material while the actual material contains two phases (filaments and the matrix). Hence, delamination in the present analysis appears as a region of removed elements rather than a re-

gion where de-bonding between adjoining phases has taken place. Despite these differences, the extent of delamination predicted by the current model appears comparable to that observed experimentally. Also, the extents of back-face bulging observed experimentally, Fig. 8(a), and the one predicted computationally, Fig. 8(b) are in reasonably good agreement. It should be noted that in the case of the computational analysis some of the elements at the composite-panel back-face in which filament failure has taken place attained a very low level of stiffness which made them undergo relatively large strains. This is the main cause of the observed “bumps” at the armor-panel back-face.

(c) In the case of a 22 mm-thick composite panel impacted by the M193 projectile at an initial velocity of 800 m/s, both the experiment, and the numerical results show only a partial penetration of the target with comparable depth of the penetration holes, Fig. 9(a) and (b). As in the case of Fig. 8(a) and (b), the present computational analysis predicts reasonably well the extent of delamination within the armor and the extent of back-face bulging. Again, low stiffness elements containing failed filaments are the main cause of the observed bumps at the armor-panel back-face, Fig. 9(b).

In his work, Iremonger [36] identified three distinct regions of composite failure when subjected to impact from the small caliber projectiles: (a) an initial penetration phase dominated by fiber shearing/cutting by the projectile and to a larger extent by plastic

deformation of the projectile; (b) extensive delamination of the composite material accompanied by destabilization and break-up/fragmentation of the projectile; and (c) extensive stretching/bulging of the armor back-face which was accompanied by extensive stretching of the fibers enabling armor to absorb substantial portion of the projectile's kinetic energy. The computational results obtained in the present work (e.g. Fig. 8(b)) clearly confirmed the existence of these three stages of projectile/composite interaction suggesting that the proposed material model for $0^\circ/90^\circ$ cross-plyed UHMWPE based armor-grade composite is physically sound.

4.3. Back-face bulge topology and temporal evolution

In Ref. [36], the temporal evolution of the composite panel back-face bulge height and diameter was reported for only one projectile/bullet/testing condition. This condition corresponds to a 32 mm thick composite test panel, the M855 bullet having an initial velocity of 900 m/s. The results obtained in Ref. [36] for the bulge height and for the bulge diameter are displayed in Fig. 10(a) and (b), respectively, and they are denoted using filled circular symbols. The corresponding computational results obtained in the present work are also displayed in these figures and they are denoted using unfilled circular symbols. A simple examination of the results displayed in Fig. 10(a) and (b) reveals that: (a)

while the initial rate of increase of the back-face bulge height predicted by the present analysis is comparable to that measured experimentally, Fig. 10(a), the computational results under predict the bulge height by ~ 5 –10 mm. There are several potential reasons for this disagreement, including: (i) the utilization of element erosion of the projectile and target in the current work; also (ii) the extents of projectile damage/fragmentation were likely different in the experiment and in the computational analysis and (iii) both the initial projectile velocity and the bulge-height measurements utilized in the work of Iremonger [36] were associated with experimental errors ranging from $\pm 5\%$; and (iii). The computed temporal evolution of the bulge-height displayed in Fig. 10(a) shows a decrease in the bulge-height after approximately 160 μs . This decrease is associated with the elastic relaxation of the composite-panel back-face after the projectile was defeated and pushed back. Similar observation was not made by Iremonger [36]. Instead, the bulge height has continued to increase, Fig. 10(a). The reason for this discrepancy is that in the work of Iremonger [36] the projectile was typically left buried within the partially penetrated armor-panel preventing back-face elastic relaxation and (b) except for the very initial stage of penetration by the projectile, the experimentally measured and computationally predicted temporal evolutions of the back-face bulge diameter are in reasonably good agreement, Fig. 10(b).

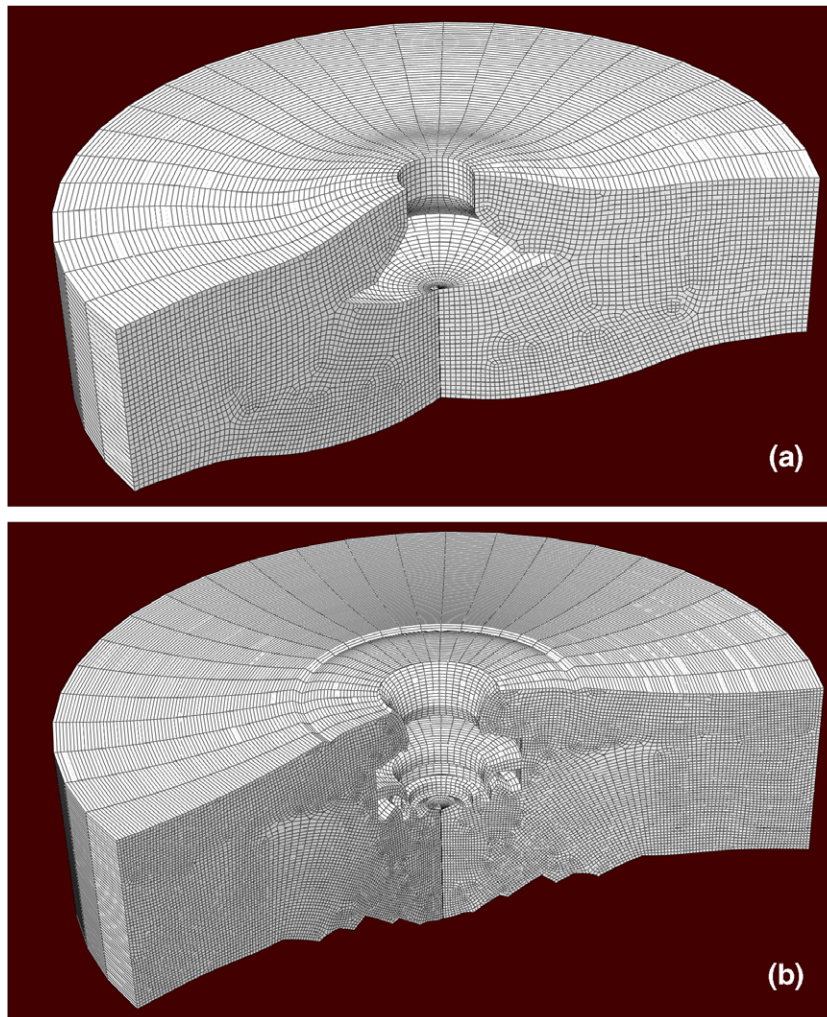


Fig. 9. A comparison between (a schematic of) the experimental results obtained in Ref. [36] (a), and their computational counterparts obtained in the present work (b), pertaining to the spatial distribution of damage in case of a M193 bullet initially propelled at a velocity of 800 m/s impacting a 22 mm thick test panel.

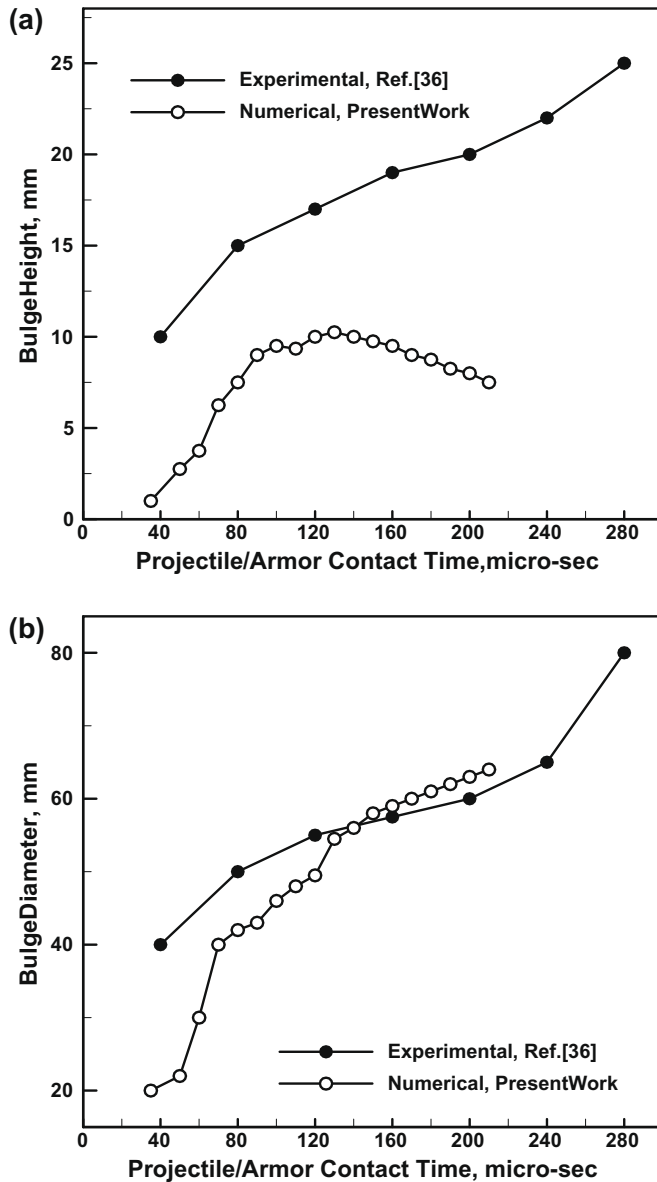


Fig. 10. A comparison between the experimental results obtained in Ref. [36] and their computational counterparts obtained in the present work pertaining to the temporal evolution of: (a) the height and (b) the diameter of a delamination-induced bulge at the composite back-face for the case of a M855 bullet initially propelled at a velocity of 900 m/s impacting a 32 mm thick test panel.

4.4. A general discussion regarding the outcome of material model validation

As stated earlier, the main objective of the present work was to develop, parameterize and validate, (against the relevant experimental results), a simple physically-based computationally-efficient continuum-level material model for a prototypical $0^\circ/90^\circ$ cross-ply oriented polyethylene fiber-based armor-grade composite material. While developing this model, unit-cell level finite-element analyses of the meso-scale material mechanical response and properties and atomic-level simulations of the filament/matrix bonding/de-bonding had to be employed giving the present approach a multi-length scale character. The relevant experimental results were taken from the work of Iremonger [36]. The material-model validation was carried out by constructing a transient non-linear dynamics finite-element model consist-

ent with the experimental setup used in the work of Iremonger [36]. The key experimental results obtained in Ref. [36] were then compared with their computational counterparts obtained in the present work to judge the validity of the present model. The obtained level of qualitative and quantitative agreement between the two sets of results suggests that the proposed material model is capable of capturing the essential behavior of a prototypical $0^\circ/90^\circ$ cross-ply UHMWPE based armor-grade composite material. While the present work was focusing on the initial development, parameterization and validation of the material model, in our future work, the model will be used to investigate in greater details the competition and interplay between various deformation, fracture and energy-dissipation phenomena which control the composite's ability to defeat projectiles by absorbing their kinetic energy.

It should be noted that the main projectile kinetic-energy absorption mechanisms suggested by Iremonger [36] and also suggested by the present investigation are based on filament cutting and filament/matrix de-bonding and delamination. As correctly pointed out by one of the reviewers of the present work, in the composite material under investigation, both the matrix and the reinforcement phases are of polymeric nature and the role of visco-elastic and inelastic (e.g. plasticity, crazing, etc.) deformation modes must be considered. The contribution of the latter energy-absorption mechanisms was also considered in the present work and it was found to be relatively small. This finding simply implies that, under high loading-rate conditions analyzed in the present work, the response of the constituent materials is dominated by their elastic behavior. While under lower and moderate loading rates, visco-elasticity and inelasticity may play significant roles in the mechanical response of the material under investigation; these roles are not significant under ballistic loading conditions.

5. Work summary and conclusions

Based on the work presented and discussed in the present manuscript, the following main summary remarks and conclusions can be drawn:

1. A simple unit-cell continuum-damage based material model for prototypical cross-ply unidirectional UHMWPE filament based armor-grade composites has been developed and parameterized.

2. To validate the model, a series of transient non-linear dynamics finite-element computations pertaining to the impact of either an armor-piercing (AP) or a non-AP 5.56 mm-caliber full-metal jacketed bullet into a 11-32 mm-thick armor test panel were carried out and the results obtained were compared with their experimental counterparts reported in Ref. [36].

3. This comparison suggested that, for the most part, the proposed model realistically accounts for the observed behavior of the cross-ply unidirectional UHMWPE filament based armor-grade composites under the specified ballistic loading conditions. The good computation/experiment agreement pertains to the success of the composite panels of different areal densities in defeating the bullets at different initial bullet velocities, post-mortem spatial distribution of damage within the panel and the temporal evolution of a bulge at the back-face of the composite.

4. The computational analysis was also able to clearly delineate three different stages of composite penetration by the projectile: (a) initial filament shearing/cutting dominated stage; (b) an intermediate stage characterized by pronounced filament/matrix de-bonding/decohesion; and (c) the final stage associated with the extensive bulging of the armor-panel back-face within which pronounced filament stretching leads to major absorption of the projectile kinetic energy.

Acknowledgements

The material presented in this paper is based on work supported by the US Army/Clemson University Cooperative Agreements W911NF-04-2-0024 and W911NF-06-2-0042.

Appendix A. Atomic-level calculations of filament/matrix bonding/de-bonding

As discussed in Section 2.1 filament/matrix bonding/de-bonding behavior and parameterization of this behavior are critical inputs to the unit-cell based finite-element calculations of the meso-scale material mechanical response. These inputs were obtained in the present work using an atomic-level (i.e. a molecular-statics based) computational analysis. Some pertinent details regarding this analysis are presented in this section. However, since the procedure used closely follows the one presented in our recent work [34], more details about the present approach can be obtained in Ref. [34].

A.1. Computational cell

An atomic-level rectangular computational cell is first constructed and filled with aligned molecules of the polyethylene (the filament material) and entangled molecules of urethane (the matrix material). One half of the computational cell was filled with one material while the other half with the other, creating a well defined filament/matrix interface. An infinite “crystal” is next constructed by applying the periodic boundary conditions to all three faces of the computational cell. The cell axes (a, b, c) are initially aligned with the three coordinate axes (x, y, z). The overall initial orientation of the filament/matrix interface was parallel with the x – y plane. The construction of the computational unit cell was done using the Amorphous Cell program from Accelrys [38]. The program allows adjustment in the cell size to obtain the desired levels of materials density. The atomic configuration within the cell is then relaxed/optimized by minimizing its potential energy.

A.2. Forcefields

It is well-established that a crucial point in the atomistic simulations of multi-particle systems is the choice of the forcefields which describe, in an approximate manner, the potential energy

hyper-surface on which the atomic nuclei move. In other words, the knowledge of forcefields enables determination of the potential energy of a system in a given configuration. In general, the potential energy of a system of interacting particles can be expressed as a sum of the valence (or bond), $E_{valence}$, cross-term, $E_{cross-term}$, and non-bond, $E_{non-bond}$, interaction energies as:

$$E_{total} = E_{valence} + E_{cross-term} + E_{non-bond} \quad (A1)$$

The valence energy generally includes a bond stretching term, E_{bond} , a two-bond angle term, E_{angle} , a dihedral bond–torsion term, $E_{torsion}$, an inversion (or an out-of-plane interaction) term, E_{oop} , and a Urey-Bradley term (involves interactions between two atoms bonded to a common atom), E_{UB} , as:

$$E_{valence} = E_{bond} + E_{angle} + E_{torsion} + E_{oop} + E_{UB} \quad (A2)$$

A schematic explanation of the first four types of valence atomic interactions is given in Fig. A1.

The cross-term interacting energy, $E_{cross-term}$, accounts for the effects such as bond length and angle changes caused by the surrounding atoms and generally includes: stretch–stretch interactions between two adjacent bonds, $E_{bond-bond}$, stretch–bend interactions between a two-bond angle and one of its bonds, $E_{bond-angle}$, bend–bend interactions between two valence angles associated with a common vertex atom, $E_{angle-angle}$, stretch–torsion interactions between a dihedral angle and one of its end bonds, $E_{end_bond-torsion}$, stretch–torsion interactions between a dihedral angle and its middle bond, $E_{middle_bond-torsion}$, bend–torsion interactions between a dihedral angle and one of its valence angles, $E_{angle-torsion}$, and bend–bend–torsion interactions between a dihedral angle and its two valence angles, $E_{angle-angle-torsion}$, terms as:

$$E_{cross-term} = E_{bond-bond} + E_{angle+angle}E_{bond-angle} + E_{end_bond-torsion} + E_{middle_bond-torsion} + E_{angle-torsion} + E_{angle-angle-torsion} \quad (A3)$$

The non-bond interaction term, $E_{non-bond}$, accounts for the interactions between non-bonded atoms and includes the van der Waals energy, E_{vdw} , the Coulomb electrostatic energy, $E_{Coulomb}$, and the hydrogen bond energy, E_{H-bond} , as:

$$E_{non-bond} = E_{vdw} + E_{Coulomb} + E_{H-bond} \quad (A4)$$

Inter- and intra-molecular atomic interactions in the filament and the matrix and between the two materials are modeled, in the present work, using COMPASS (Condensed-phased Optimized Molecular Potential for Atomistic Simulation Studies), the first *ab initio* forcefield that enables an accurate and simultaneous predic-

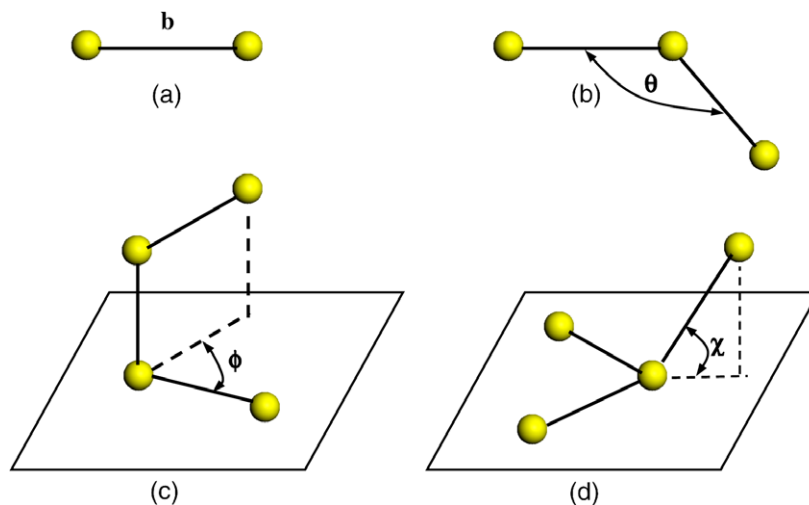


Fig. A1. A schematic of the: (a) stretch; (b) angle; (c) torsion; and (d) inversion valence atomic interactions.

tion of various gas-phase and condensed-phase properties of organic and inorganic materials [39,40]. The specific functional forms for Eqs. (A1)–(A4) as defined within the COMPASS forcefield can be found in Ref. [34].

A.3. Computational method

Determination of the filament/matrix bonding/de-bonding behavior at the atomic-level was accomplished in the present work by subjecting the computational cell to an appropriate deformation mode followed by potential-energy minimization of the cell with respect to the atomic positions and the *free* computational-cell edge lengths and angles (molecular statics simulations). During these simulations, the potential energy of the cell is recorded and the atomic microstructure closely monitored for the onset of de-bonding. Two modes of deformations were used: (a) uni-axial tension in the direction normal to the filament/matrix interface and (b) simple shear in a direction parallel with the filament/matrix interface. All the molecular statics simulations are carried out using the Discover program by Accelrys [41].

The potential energy minimization within Discover is carried out by combining the Steepest Descent, Conjugate Gradient and the Newton's minimization algorithms. These algorithms are automatically inactivated/activated as the atomic configuration is approaching its energy minimum (i.e. the Steepest Descent method is activated at the beginning of the energy minimization while the

Newton's method is utilized in the later stages of the simulation). Deformation of the computational cell was carried out using a Discover input file which is written in a BTCL (Basic Tool Command Language) language. This enabled the use of a scripting engine that provides very precise control of simulation jobs, e.g. a cell deformation to be carried out in small steps each followed by energy minimization. To help prevent the computational crystal from settling into a nearby metastable higher-energy configuration, a 10,000-step 298 K NVT molecular dynamics run was introduced between the cell deformation and the energy minimization steps. An example of the initial and deformed configurations of the computational cell is shown in Fig. A2(a) and (b).

The procedure described above yielded a plot of the potential energy increase (relative to that in the initial optimized computational cell) vs. the extension Δc of the computational cell in the *z*-direction. The gradient of the potential energy increase with respect to the change in the *controlled* computational-cell parameter (i.e. the edge length or the angle) normalized by the appropriate loaded cross sectional area is then used to determine the corresponding normal/shear stress associated with the given deformation mode. Likewise, properly normalized changes in the cell parameters are used to compute the corresponding cell strain(s) (i.e. interfacial displacement-discontinuities).

Using the aforementioned procedure, it was possible to construct the previously-defined (linear) filament/matrix interfacial traction vs. interfacial displacement–discontinuity/strain relations

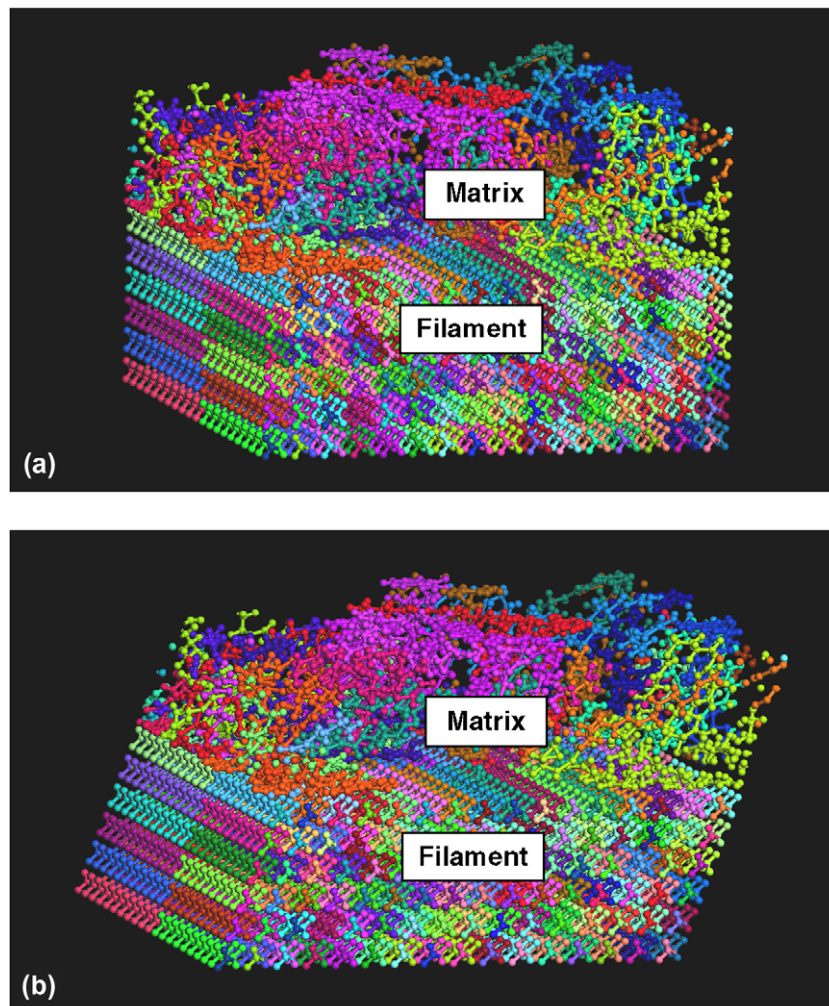


Fig. A2. An example of the: (a) initial and (b) deformed atomistic computational cell used in molecular statics analysis of the filament/matrix bonding/de-bonding behavior.

(one for the normal and one for the shear deformation modes) both during elastic re-loading/unloading and loading associated with interfacial damage. For each of the two deformation modes, these relations are characterized by three parameters: (a) a critical normal or shear interfacial displacement–discontinuity/strain at which damage initiation begins; (b) the corresponding normal or shear traction (i.e. the interfacial strengths); and (c) a normal or shear interfacial displacement–discontinuity/strain at which complete filament/matrix decohesion takes place.

References

- [1] ANSYS/Autodyn version 11.0, User Documentation, Century Dynamics Inc. a subsidiary of ANSYS Inc.; 2007.
- [2] ABAQUS version 6.7, User Documentation, Dassault Systems; 2007.
- [3] Lee BL, Song JW, Ward JE. Failure of spectra[®] polyethylene fiber-reinforced composites under ballistic impact loading. *J Compos Mater* 1994;28(13):1202–26.
- [4] Lee BL, Walsh TF, Won ST, Patts HM, Song JW, Mayer AH. Penetration failure mechanisms of armor-grade fiber composites under impact. *J Compos Mater* 2001;35:1605–35.
- [5] Donovan JG, Kirkwood B, Figucia F. Development of lower cost ballistic protection. US Army Natick RD&E Center, Natick, MA, Technical report Natick/TR-85/019L; 1985.
- [6] Lin LC, Bhatnagar A, Chang HW. Ballistic energy absorption of composites. In: *Proc 22rd SAMPE Int Tech Conf*; 1990. p. 1–13.
- [7] Prevorsek DC, Kwon YD, Chin HB. Analysis of the temperature rise in the projectile and extended chain polyethylene fiber composite armor during ballistic impact and penetration. *Polym Eng Sci* 1994;34:141–52.
- [8] Zhu G, Goldsmith W, Dharan CKH. Penetration of laminated Kevlar by projectiles. I. Experimental investigation. *Int J Solids Struct* 1992;29(4):399–420.
- [9] Zhu G, Goldsmith W, Dharan CKH. Penetration of laminated Kevlar by projectiles. II. Analytical model. *Int J Solids Struct* 1992;29(4):421–4.
- [10] Schuman TL. S2000 ballistic hardened C31 shelter. In: *Proc 24th SAMPE Int Tech Conf*; 1992. p. 280–90.
- [11] Segal CL. High-performance organic fibers, fabrics and composites for soft and hard armor applications. In: *Proc 23rd SAMPE Int Tech Conf*; 1991. p. 651–60.
- [12] Riewald PG, FolgarYang FHH, Shaughnessy WF. Lightweight helmet from a new aramid fiber. In: *Proc 23rd SAMPE Int Tech Conf*; 1991. p. 684–95.
- [13] Thomas TS. Facets of a lightweight armor system design. In: *Proc 22rd SAMPE Int Tech Conf*; 1990. p. 304–18.
- [14] Prevorsek DC, Chin HB. Development of a lightweight spectra helmet. Phase I interim technical report from AlliedSignal Inc. to US Army Natick RD&E Center, Natick, MA, DAAK60-87-C-0089/D; 1988.
- [15] Song JW, Egglestone GT. Investigation of the PVB/PF ratios on the crosslinking and ballistic properties in glass and aramid fiber laminate systems. In: *Proc 19th SAMPE Int Tech Conf*; 1987. p. 108–19.
- [16] Smith JC, Blandford JM, Schiefer HF. Stress–strain relationships in yarns subjected to rapid impact loading: part VI. Velocities of strain waves resulting from impact. *Text Res J* 1960;30(10):752.
- [17] Smith JC, Blandford JM, Towne KM. Stress–strain relationships in yarns subjected to rapid impact loading: part VIII. Shock waves limiting breaking velocities and critical velocities. *Text Res J* 1962;32(1):67.
- [18] Roylance D, Wilde A, Tocci G. Ballistic impact of textile structures. *Text Res J* 1973;43:34–41.
- [19] Cunniff PM. An analysis of the system effects in woven fabric under ballistic impact. *Text Res J* 1992;62(9):495–509.
- [20] Dent RW, Donovan JG. Projectile impact with flexible armor—an improved model. US Army Natick RD&E Center, Natick, MA, Technical report Natick/TR-86/044L; 1986.
- [21] Hsieh CY, Mount A, Jang BZ, Zee RH. Response of polymer composites to high and low velocity impact. In: *Proc 22nd SAMPE Int Tech Conf*; 1990. p. 14–27.
- [22] Critescu N, Malvern LE, Sierakowski RL. Failure mechanisms in composite plates impacted by blunt-ended penetrators. Foreign object impact damage to composites. Philadelphia (PA): ASTM; 1975. p. 159–72 [ASTM STP #568].
- [23] Cairns DS, Lagace PA. Transient response of graphite/epoxy and Kevlar/epoxy laminates subjected to impact. *AIAA J* 1989;27(11):1590–6.
- [24] Frissen R, Peijs T, Verlinde A. In: *16th Int Symp Ballistics*, San Francisco, September; 1996.
- [25] Cunniff PM. In: *Proc 18th Int Symp Ballistics*, San Antonio, November; 1999. p. 1303.
- [26] Clegg R, Hayhurst C, Leahy J, Deutekom M. In: *Proc 18th Int Symp Ballistics*, San Antonio, November; 1999. p. 791.
- [27] Floyd AM, Williams K, Varziri R, Kanji K, Pourtasip A. In: *Proc 18th Int Symp Ballistics*, San Antonio, November; 1999. p. 877.
- [28] Cunniff PM, Ting J. In: *Proc 18th Int Symp Ballistics*, San Antonio, November; 1999. p. 822.
- [29] Johnson GR, Beissel R, Cunniff PM. In: *Proc 18th Int Symp Ballistics*, San Antonio, November; 1999. p. 862.
- [30] Guan X, Birnbaum N. In: *Proc 18th Int Symp Ballistics*, San Antonio, November; 1999. p. 1107.
- [31] Jacobs MJN, Van Dingenen JJJ. Ballistic protection mechanisms in personal armour. *J Mater Sci* 2001;36:3137–42.
- [32] Grujicic M, Arakere G, He T, Bell WC, Cheeseman BA, Yen C-F, et al. A ballistic material model for cross-plyed unidirectional ultra-high molecular-weight polyethylene fiber-reinforced armor-grade composites. *Mater Sci Eng A*, in press.
- [33] Jacobs MJN, Beugels JHM, Blaauw M. Process for the manufacture of a ballistic-resistant moulded article. US Patent 7,288,314 B2, October; 2007.
- [34] Grujicic M, Sun YP, Koudela KL. The effect of covalent functionalization of carbon nanotube reinforcements on the atomic-level mechanical properties of poly-vinyl-ester-epoxy. *Appl Surf Sci* 2007;253:3009.
- [35] Cheeseman BA, Bogetti TA. Ballistic impact into fabric and compliant composite laminates. *Compos Struct* 2003;61:161–73.
- [36] Iremonger MJ. Polyethylene composites for protection against high velocity small arms bullets. In: *Int Symp Ballistics*, San Antonio, November; 1999. p. 946–53.
- [37] Grujicic M, Pandurangan B, Zecevic U, Koudela KL, Cheeseman BA. Ballistic performance of alumina/S-2 glass-reinforced polymer-matrix composite hybrid lightweight armor against armor piercing (AP) and non-AP projectiles. *Multidiscipline Model Mater Struct* 2007;3:287–312.
- [38] <http://www.accelrys.com/mstudio/msmodeling/amorphouscell.html>.
- [39] Sun H. Condensed-phased optimized molecular potential for atomistic simulation studies. *J Phys Chem B* 1998;102:7338.
- [40] Sun H, Ren P, Fried JR. Condensed-phased optimized molecular potential for atomistic simulation studies. *Comput Theor Polym Sci* 1998;8(1/2):229.
- [41] <http://www.accelrys.com/mstudio/msmodeling/discover.html>.